UNIVERSITY OF GRONINGEN

university of groningen

BACHELOR THESIS

Modelling the Dark Matter Halos of Galaxies at z∼1 Through Rotation Curve Decomposition

Author:
Nikki POTZE

Supervisors:
Prof. dr. Filippo FRATERNALI
M.Sc. Pavel MANCERA PIÑA
2nd Examiner:
Dr. Manuela VECCHI

Abstract

Studies of galactic rotation curves have revealed a significant discrepancy between the dynamical and the luminous mass in disc galaxies. The existence of large non-baryonic dark matter halos was inferred to explain the absence of the expected Keplerian fall. In this work, the method of rotation curve decomposition was used in an attempt to reconstruct the dark matter halos of a sample of disc galaxies at $z \sim 1$. First, Hα intensity maps and HST images were analysed to determine the gas and stellar contributions to the rotation curves, respectively. Then, observed rotation curves obtained with KMOS were used in a MCMC routine to fit and constrain the virial masses of the dark matter halos. Reduced chi-squares of our fits range from 0.66 to 15.80. Galaxies for which the observed rotation curves were well reproduced, returned halo masses consistent with the stellar-to-halo mass relation determined at $z \sim 1$ by other authors using independent techniques.

Kapteyn Astronomical Institute

Friday 18th December, 2020

Contents

Acknowledgements

Foremost, I would like to express my sincere graditute towards Filippo Fraternali and Pavel Mancera Piña for providing me with this interesting project, and for finding the time in their busy schedules to supervise me as well as they did. Secondly, I thank Thijs Luggenhorst for being a friend and providing a place to share thoughts and ideas, it helped me a lot.

With the closing of the University of Groningen due to COVID-19, a great part of my social network also closed. I found comfort in writing while the outside world was shutting down. To compensate for the lack of personality in a scientific thesis, I add a short poem, to make it mine.

I once was bothered by the motion
of all around and all above

I turned to knowledge page by page
learned while and why the sky changed color

found motivation in a sentence
brought peace to a restless mind

to do as you like is never to please

I put in orbit, that which matters
repeated until I too could hear

the Sun
the Moon
the Earth

and all that surrounds

Chapter 1

Introduction

One of the greatest enigmas in our universe is the existence of dark matter. Dark matter does not absorb, reflect or emit electromagnetic radiation and therefore cannot be observed directly. Whilst dark matter does not emit radiation, it does interact gravitationally with visible matter. Dark matter exerts gravitational forces on luminous matter and from the resulting effects, its existence has been inferred. The theory of dark matter provides a solution to unexplained motions of stars and galaxies amongst other objects in the universe. Within the scientific community, dark matter is presumed to consist of non-baryonic particles (Steigman et al. 1978; Faulkner and Gilliland 1985) and accounts for most of the matter in the Universe (Planck Collaboration, Aghanim, et al. 2020).

It has long been suggested that galaxies form at the center of dark matter halos (Rees and Ostriker 1977; Fall and Efstathiou 1980; Blumenthal et al. 1984). The clumping and merging of dark matter in the early Universe supposedly provided the gravity for protogalactic clouds to contract, and eventually form galaxies (S. D. M. White and Rees 1978). By studying dark matter halos we gain a better understanding of the physics of galaxy formation and evolution in our Universe. By gaining insight into the cosmology of the early Universe and the role of dark matter in galaxy formation, we can begin to understand how we got to where we are today.

1.1 Rotation curves

The key observational evidence for the existence of non-luminous (dark) matter, is the shape of galactic rotation curves (van Albada and Sancisi 1986). Rotation curves are plots that set out the rotational velocity of a galaxy against the galactocentric distance. A typical rotation curve is shown in Figure 1.1. The shape of a rotation curve is readily related to the galactic potential and depends on the mass distribution in the galaxy.

It is important to note the distinction between rotational and circular speed of a galaxy. Whilst the rotational velocity ($v_{\rm rot}$) is the average velocity of a certain matter component of the galaxy (e.g., gas or stars) at a given distance from the center, the circular speed ($v_{\rm c}$) is a mathematical concept that can be defined in any system. The circular speed represents the speed a particle would have at a certain location given the gravitational potential of the system. Assuming spherical symmetry, the gravitational potential and circular speed of a galaxy are related by:

$$\frac{d\Phi(r)}{dr} = \frac{v_{\rm c}^2(r)}{r} = \frac{GM(r)}{r^2}, \tag{1.1}$$

where $\Phi(r)$ is the gravitational potential, $v_{\rm c}(r)$ the circular speed, r the radius and $M(r)$ the mass contained within radius r. In reality, the observed rotation velocity $v_{\rm rot}$ of a matter component in a galaxy does not solely depend on the galactic potential, but is also influenced by the gas and the turbulent pressure. Thus, to derive the circular speed, the rotation of a matter component must be corrected for the potential pressure support, this is called the asymmetric drift correction (Binney and Tremaine 2008). However, when galaxies are rotating with speeds > 100 km/s, one can typically assume negligibly small asymmetric drift corrections. We also make this assumption for the continuation of this thesis. Accordingly, the circular speeds inside the galaxy will be represented by the observed rotation curves, such that $v_{\rm c} = v_{\rm rot}$.

When considering a typical exponential stellar disc, we expect to see a decrease in rotational velocity as we move outwards from the center of the galaxy. This is analogous to considering a galaxy with a roughly constant mass M beyond a certain radius. In this case we expect to see a Keplerian fall, described by:

$$v_{\text{rot}}(r) \approx \sqrt{\frac{GM}{r}} \propto r^{-1/2}, \tag{1.2}$$

Remarkably, this decline is not observed. Instead, observations generally show a flat rotation curve up to large radii (Bosma 1978; Rubin, Ford, and Thonnard 1980; van Albada and Sancisi 1986), which implies that the galactic mass increases linearly with radius, suggesting the presence of a large dark matter halo (Zwicky 1933; Colless and Dunn 1996), as shown in Figure 1.1.

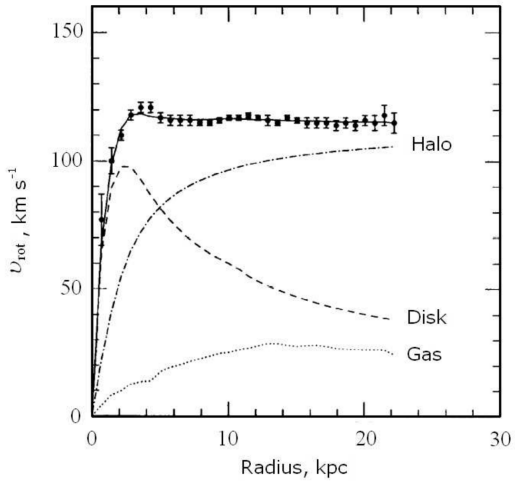

Figure 1.1: The dots represent the rotation curve of spiral galaxy NGC 6503. The baryonic components of the galaxy are not sufficient to reproduce the outer parts of the rotation curve. Figure taken from Doroshkevich, Lukash, and Mikheeva 2012, with data from Freese 2009.

1.1.1 Emission line observations as kinematical tracers

Rotation curves of disc galaxies can be obtained using spectroscopic data from emission line observations. Atoms and molecules emit radiation when transitioning from high to low energy states. Specific transitions lead to emission lines with known rest-frame wavelengths. Some of the most used spectral lines are the 21-cm hyperfine line of neutral hydrogen (HI), the recombination lines of ionized hydrogen (e.g., Hα) and the ro-vibrational lines of carbon monoxide (CO).

Hα is a spectral line from the Balmer series with a rest-frame wavelength of 656.28 nm. It occurs when the electron in a hydrogen atom falls from its third to second lowest energy level. In star-forming regions, hydrogen atoms are constantly being ionized by UV photons produced by young massive stars. Whenever an atom is ionized, it can recombine with a free electron. The electron then cascades down to lower energy states, whilst emitting radiation. Observing this emission indicates that hydrogen is being ionized, which is an effective probe of finding star formation regions and also tells us about the distribution of the hydrogen present in the galaxy. In this project, the Hα spectral line will be used as both a kinematical and a gas density tracer.

To gain information about the rotational velocity of galaxies from their spectra, one can make use of the Doppler effect. The Doppler effect occurs when there is relative motion between emitter and observer, which is the case for a rotating external galaxy. As a consequence of rotation, a disc oriented in the sky will be approaching on one side (with respect to Earth), and receding on the other. Electromagnetic radiation emitted by the baryonic components of the approaching side of the galaxy is "compressed", causing the observed spectral lines to shift towards shorter wavelengths (blueshifted). Whereas radiation emitted by the receding side of the galaxy is "stretched out", causing the spectrum to appear more red (redshifted). From the amount of shift of the characteristic spectral lines with respect

to their rest-frame wavelengths, the rotational speed of galaxies can be reconstructed.

When detecting Hα emission from galaxies at redshift $z \sim 1$, we expect to observe the Hα spectral line to appear redshifted to a value of around 1312.56 nm, according to the relation:

$$\frac{\lambda_{\text{obs}}}{\lambda_{\text{emit}}} = 1 + z, \tag{1.3}$$

where λ_{obs} and λ_{emit} are the observed and emitted wavelengths, respectively. This shift is called the cosmological redshift and is due to the expansion of the Universe. However, when there is additional relative motion, such as the rotation of a galaxy, we see fluctuations from the expected redshifted wavelength. From these fluctuations, the rotational velocity of the galaxy can be derived.

In the same way as described above, the CO spectral line serves as a tracer for molecular gas and the tracer for neutral atomic hydrogen gas at $z = 0$ is typically the 21-cm line. Due to limitations of current instruments, galaxies in the high-redshift Universe cannot be observed in HI, which is why other lines, like Hα and CO, are used instead. By means of measuring the Doppler shifts of the spectral lines at various locations of the galaxy, one can reconstruct its velocity field. Through the analysis of these velocity fields, the rotation curve of the galaxy can be derived. An example of a velocity field of a galaxy is shown in Figure 1.2.

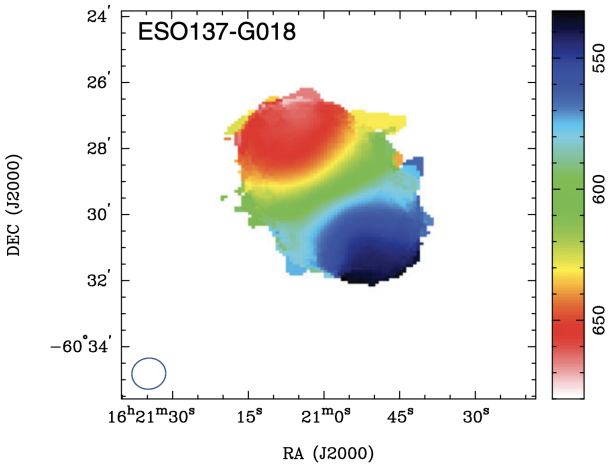

Figure 1.2: Observed HI velocity field of the local irregular dwarf galaxy ESO137-G018 (Kirby et al. 2012).

1.2 Rotation curve decomposition

Rotation curve decomposition is a method in which galactic rotation curves are used to determine the mass profiles of the various matter components. The concept of rotation curve decomposition is based on the knowledge that the circular speed of a galaxy is a direct reflection of its galactic potential. The gravitational potential of the galaxy is the sum of the contributions by the various mass components that make up the total galactic mass. In this thesis, we consider three mass components: the stellar disc, the gaseous disc and the dark matter halo. Expressed in velocities, this sum becomes:

$$v_{\text{rot}}^2 = v_*^2 + v_{\text{g}}^2 + v_{\text{h}}^2, \tag{1.4}$$

where v_*, v_{g} and v_{h} are the stellar, gas and dark matter halo contributions to the rotation curve respectively (recalling the assumption $v_{\text{c}} = v_{\text{rot}}$). For each of the mass components, appropriate fitting functions must be employed in order to reconstruct the observed rotation curves.

1.3 Baryonic contributions

To determine the baryonic contributions to the rotation curve, the stellar and gaseous discs must be reconstructed. In order to do this, one must have information on both the the total mass of the discs

and the distribution of this mass (i.e., the shapes of the discs). By tracing the surface brightness profiles and relating them to the mass surface densities, the shapes of the discs can be determined. If the total mass is known, it can be used to normalize the determined shape and so the disc surface densities can be constructed. The corresponding potentials can be derived using mathematical tools. Having derived the potentials, one can infer their circular speeds and hence their contributions to the observed rotation curve.

At $z = 0$ the surface density of a gaseous disc is typically dominated by molecular hydrogen (H_2) in the center and neutral hydrogen (HI) in the outer regions. Unfortunately, as described earlier, galaxies at $z \sim 1$ cannot currently be observed in neutral hydrogen. As a solution, the mass can be estimated using scaling relations, as we will explain in Section 3.3.2. Since Hα observations in the high-redshift Universe are feasible, Hα can in principle serve as a tracer for the gas distribution, even though the mass is not dominated by ionized hydrogen.

1.4 Dark matter halo

Studies have shown that observed rotation curves can be reproduced by considering a dark matter halo. Dark matter halos can be described by various functional forms such as the pseudo-isothermal halo (van Albada and Sancisi 1986; Kormendy and Freeman 2004), the Einasto profile (Einasto and Haud 1989) and the Navarro-Frenk-White profile (Navarro, Frenk, and Simon D. M. White 1996). The latter is one of the most commonly used density profiles to model dark matter halos and will also be used in this thesis.

1.4.1 Navarro-Frenk-White profile

The Navarro-Frenk-White (NFW) profile describes a spherically symmetric density profile which very well fits the shapes of dark matter halos produced by N-body cosmological simulations (Navarro, Frenk, and Simon D. M. White 1996). In principle, the NFW halo is described by two parameters: the scale radius r_s and the corresponding density ρ_s. The density distribution is given by

$$\rho(r) = \frac{4\rho_s}{(r/r_s)(1 + r/r_s)^2}, \tag{1.5}$$

This relation can also be expressed using two characteristic parameters; the concentration c_Δ and the virial mass M_Δ. Nevertheless, dark matter-only simulations found that these two are not independent, but related by

$$M_\Delta = 4\pi\rho_s r_s^3 A(c_\Delta), \qquad A(c_\Delta) \equiv \ln(1 + c_\Delta) - \frac{c_\Delta}{1 + c_\Delta} \tag{1.6}$$

(Bullock et al. 2001). Here Δ is the critical overdensity for virialisation. A widely adopted choice for this parameter is $\Delta = 200$ (Cimatti, Filippo Fraternali, and Nipoti 2020), independent of redshift; for simplicity we maintain this choice of parameter. The concentration of the halo is then defined as $c_\Delta = c_{200} = \frac{r_{200}}{r_s}$, where r_{200} is the virial radius; the radius enclosing an average density equal to 200 times the critical density of the universe. The critical density of the universe is the average density required in order to *just* halt its expansion, but only after an infinite time. A universe with the critical density is said to be flat. The critical density is dependent on the Hubble parameter and therefore on redshift. Values for the critical density are 13.60×10^{10} $M_\odot Mpc^{-3}$ and 4.9×10^{10} $M_\odot Mpc^{-3}$ at $z = 0$ and $z = 1$, respectively[1].

One can determine the circular speed of the NFW profile using the following equation:

$$v_{NFW}(r) = v_{200}\sqrt{\frac{\ln(1 + c_{200}x) - \frac{c_{200}x}{1+c_{200}x}}{x\ln(1 + c_{200}) - \frac{c_{200}}{1+c_{200}}}} \tag{1.7}$$

where $x = r/r_s$.

[1] https://cosmocalc.icrar.org/

1.4.2 Concentration-mass-redshift relation

As seen earlier, a NFW dark matter halo has two main parameters, the virial mass (M_{200}) and the concentration (c_{200}). Cosmological N-body simulations (Ludlow et al. 2014) found that the relation between the concentration and virial mass of the halo is well approximated by a power law:

$$\log c_{200} = a + b \log\left(\frac{M_{200}}{10^{12} h^{-1} M_\odot}\right), \tag{1.8}$$

where $a = a(z)$ and $b = b(z)$ are redshift-dependent parameters and $h = h(z)$ is the Hubble parameter. This relation is called the concentration-mass-redshift relation. Using this relation, there is one free parameter left to fit in order to get the density distribution of the dark matter halo. In this project, we assume the dark matter halos of our galaxies to follow precisely this relation, although scatter around it has been reported (Dutton and Macciò 2014; Li et al. 2020). Taking the virial mass as a free parameter, one can let the concentration of the halo follow from Eq. 1.8. In this equation, values for $a(z)$ and $b(z)$ have been taken to be $a = 0.728 \pm 0.001$ and $b = -0.073 \pm 0.001$ to fit NFW profiles at redshift 1 with $\Delta = 200$ (Dutton and Macciò 2014).

1.4.3 Stellar-to-halo mass relation

Another relation used in this work, is the stellar-to-halo mass relation (SHMR). From the SHMR and its evolution, we gain insight on the process of galaxy formation. A linear model for the SHMR is given by

$$\log \frac{M_*}{M_{200}} = \alpha \log \frac{M_*}{M_\odot} + \log f_0, \tag{1.9}$$

where M_* and M_{200} are the stellar mass and halo mass, respectively. Parameters and their 68% confidence intervals for this relation are determined to be $\log f_0 = -5.3^{+0.7}_{-0.7}$ and $\alpha = 0.35^{+0.07}_{-0.07}$, at $z = 0$ (Posti et al. 2019).

Moster et al. 2010 proposed a SHMR described by a double power-law:

$$\frac{M_*}{M_{200}}(z) = 2A(z)\left[\left(\frac{M_{200}}{M_A(z)}\right)^{-\beta(z)} + \left(\frac{M_{200}}{M_A(z)}\right)^{\gamma(z)}\right]^{-1}, \tag{1.10}$$

where $M_A(z)$ is the characteristic halo mass at the specified redshift. Girelli et al. 2020 parameterized this SHMR and reported parameters and their 68% confidence intervals to be $A = 0.0429^{+0.0018}_{-0.0017}$, $M_A = 12.03^{+0.06}_{-0.05}$, $\beta = 0.99^{+0.15}_{-0.13}$ and $\gamma = 0.638^{+0.014}_{-0.014}$, in range $0.80 < z < 1.10$.

1.5 This thesis

The use of galaxy kinematics to decompose rotation curves has long been a primary method for investigating the mass components of galaxies. This has been done extensively at redshift 0. However, such rotation curve decomposition in the high-redshift universe is a relatively new area of science (Rizzo et al. 2020). Thanks to large spectroscopic observations with various instruments (in particular SINFONI, KMOS, ALMA), data cubes containing spectroscopic data of many galaxies in the high-redshift universe have been made available to study (Förster Schreiber et al. 2009; Wisnioski et al. 2015; Neeleman et al. 2020). Having access to this spectroscopic information, we can derive rotation curves for galaxies at redshifts higher than 0.

In this thesis, we attempt to model dark matter halos of galaxies at $z \sim 1$ by performing rotation curve decomposition. The aim is to reconstruct existing, observed Hα rotation curves by fitting stellar, gas, and dark matter halo mass components. Firstly, we consider the stellar component and the gaseous disc. After this, the non-baryonic, dark matter halo, will be inferred. The galaxies for the rotation curve study presented here have been selected from the 18 $z \sim 1$ galaxies previously studied by Di Teodoro, F. Fraternali, and Miller 2016 (hereafter TFM16) and Marasco et al. 2019.

This thesis is structured as follows. After having covered the necessary theory, we introduce our galaxy sample in Chapter 2. In Chapter 3, the methods used and assumptions made to get to our results are described. After this, the results will be stated and discussed in Chapter 4. Finally, we present our conclusions in Chapters 5.

Throughout this work, we adopt a flat ΛCDM cosmology, with parameters $\Omega_{m,0} = 0.27$ and $\Omega_{\Lambda,0} = 0.73$ (Planck Collaboration, Fermi Collaboration, et al. 2015) and $H_0 = 70$ km s^{-1} Mpc^{-1}, in accordance with the studies in the literature used alongside the text.

Chapter 2

Data sample

For this work, we selected a subsample from these 18 galaxies. Our subsample initially contained the 7 galaxies with rotation curves that had relatively high spatial resolution (values at 4 radii). To further test our method, we rounded the sample to a total of 10, by including galaxies with rotation curves consisting of 3 radii. The second selection criterion required no bright star forming regions displaced from the center of the galaxy, which would make the radial profiles more uncertain.

All galaxies in our sample have been observed by the Hubble Space Telescope (HST). The F814w-filter HST image, total Hα flux map, and the Hα velocity field of a representative galaxy of our sample is shown in Figure 2.1. For similar images of the remaining galaxies in our sample, we refer to TFM16. All galaxies in our sample belong to large surveys of well-studied fields, such as the Cosmological Evolution Survey (COSMOS), the Ultra Deep Survey (UDS), and the Great Observatories Origins Deep Survey (GOODS).

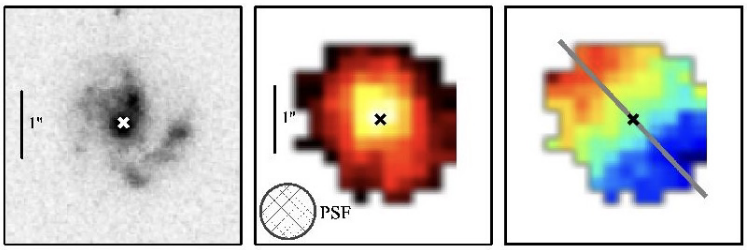

Figure 2.1: Visual representations of properties of galaxy $zcos\_z1\_692$. The left panel shows the HST image in the F814w-filter from the CANDELS survey (Grogin et al. 2011). The middle and right panels show the total Hα intensity map and the Hα velocity field, respectively. The white and black crosses denote the centers adopted in the fit, the empty circle denotes the PSF and the grey line on the velocity field displays the kinematic position angle. Figure taken from TFM16.

Stellar masses of the galaxies in our sample have been taken from TFM16. For the galaxies in the GOODS-S and UDS fields, the stellar masses have originally been acquired by the Cosmic Assembly Near-infrared Deep Extragalactic Legacy Survey (CANDELS; Grogin et al. 2011; Koekemoer et al. 2011). They are averages obtained by usage of various estimators (Santini et al. 2015). Stellar masses of the galaxies in the COSMOS field, have been taken from either the COSMOS or 3D-HST catalogs and are derived using the Fitting and Assessment of Synthetic Templates (FAST; Kriek et al. 2009). The stellar masses of the galaxies in our sample have associated uncertainties, since different studies (e.g., Stott et al. 2016) report notably different values for these masses.

Stellar surface brightness profiles of our galaxies have been obtained from Marasco et al. 2019. Inclinations, kinematic centers, and cosmological redshifts of the galaxies could be taken from TFM16. Position angles of the galaxies could be extracted from the headers of the data cubes from KROSS.

Name	Field	RA (J2000) h m s	Dec (J2000) ° ′ ″	z	$\log M_*/M_\odot$
gs3_22005†	GOODS-S	03 32 29.85	−27 45 20.5	0.954	10.72 ±0.12
hiz_z1_195	COSMOS	10 00 34.63	+02 14 29.5	0.856	9.75 ±0.09
u3_5138†	UDS	02 16 59.89	−05 15 07.6	0.809	9.74 ±0.12
u3_25160†	UDS	02 17 04.69	−05 09 46.4	0.897	10.05 ±0.15
zcos_z1_202	COSMOS	10 00 53.39	+01 52 40.8	0.841	10.54 ±0.06
zcos_z1_692	COSMOS	10 00 36.42	+02 11 19.2	0.930	10.61 ±0.18
zmus_z1_21	GOODS-S	03 32 48.48	−27 54 16.0	0.839	10.40 ±0.14
zmus_z1_119	GOODS-S	03 32 08.20	−27 47 52.1	0.840	10.34 ±0.07
zmus_z1_166	GOODS-S	03 32 16.49	−27 44 49.1	0.975	10.11 ±0.15
zmus_z1_217	GOODS-S	03 32 20.51	−27 40 58.9	0.895	10.02 ±0.08

Table 2.1: Table showing specifics of the galaxies in our sample. From left to right: name adopted in the main survey, field, Right Ascension in J2000, Declination in J2000, spectroscopic redshift, stellar masses taken from TFM16. Galaxies belonging to the KMOS3*D* survey are marked (†), the remaining galaxies belong to the KROSS survey.

Upon inspection, some of them were slightly adjusted to show good agreement with the corresponding values from TFM16. For the KMOS3*D* galaxies, the position angles were directly adopted from TFM16. Tables 2.1 and 3.1 show overviews of the properties of the galaxies in our sample.

To derive the gas contribution in our rotation curves, we make use of Hα emission maps. Some of the galaxies from our sample are part of the KROSS survey, their Hα maps could be directly downloaded from the KROSS website[1]. For the remaining galaxies, part of the KMOS3*D* survey, we used the data cubes to build the Hα maps.
Data cubes for the remaining galaxies could be downloaded from the KMOS3*D* website[2]. Having identified the channel maps containing the Hα emission, the cubes could be sliced and processed using software $^{3D}Barolo$ (Di Teodoro and F. Fraternali 2015) and standard Astropy routines, as we will discuss shortly.

[1] http://astro.dur.ac.uk/KROSS/data.html
[2] https://www.mpe.mpg.de/ir/KMOS3D

Chapter 3

Methodology

3.1 $^{3D}Barolo$

In this project, we make use of the software $^{3D}Barolo$[1] . The $^{3D}Barolo$ algorithm is mainly designed to fit 3D tilted-ring models to spectroscopic data cubes in order to derive the kinematics of galaxies (Di Teodoro and F. Fraternali 2015). However, $^{3D}Barolo$ provides various tasks that can be used to adapt to the user's needs. In this project, we utilize tasks TOTALMAP and ELLPROF.

As mentioned in Chapter 2, $^{3D}Barolo$ was used to obtain the Hα intensity maps of some of our galaxies. $^{3D}Barolo$ takes in the data cubes and outputs an Hα intensity map by setting task TOTALMAP to true. Once we acquired Hα maps of all galaxies in our sample, we utilized $^{3D}Barolo$'s task ELLPROF to obtain radial surface brightness profiles.

The ELLPROF task is based on the homonymous task from GIPSY (Groningen Image Processing System; Allen et al. 2011) and needs several parameters to run. For each galaxy, the center (XPOS, YPOS), position angle (PA), inclination (i), the number of rings to be used (NRADII), and their spatial separation (RADSEP) were listed in a parameter file, together with the Hα intensity map of the galaxy. Task ELLPROF takes this file and calculates the projection on the sky of the tilted rings (ellipses) at the specified radii. It then computes the average value within the ellipses and creates an output file containing the surface brightness as a function of radius.

For consistency, we used the same amount of rings in our surface brightness profiles as there are points in the rotation curves from TFM16, considering that the same data cubes were used to derive these rotation curves. We choose RADSEP such that the rings extend as far as the rotation curves do. Upon inspection of the fitted ellipses, we adopted slightly different centers for some of the galaxies. A visualization of the rings fitted by ELLPROF can be seen as the red rings in Figure 3.1. A complete overview of parameters used in $^{3D}Barolo$ to obtain the surface brightness profiles, is presented in Table 3.1.

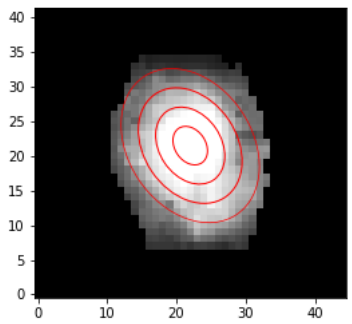

Figure 3.1: Vizualisation of the ellipses fitted by task ELLPROF in $^{3D}Barolo$ on galaxy $zcos\_z1\_692$. The rings have a spatial separation of 2.4 kpc (0.3"). The outer ring is located at a distance of 8 kpc (1") from the center, which is as far as the rotation curve used in this work extends.

[1] https://editeodoro.github.io/Bbarolo/

Name	NRADII	RADSEP	XPOS	YPOS	i	PA
		"	*pixels*	*pixels*	°	°
gs3_22005	4	0.30	9.0	9.5	47	40
hiz_z1_195	3	0.30	22.8	20	49	1
u3_5138	4	0.28	8.75	8	62	1
u3_25160	4	0.28	12	11	53	35
zcos_z1_202	4	0.22	21	21.5	45	20
zcos_z1_692	4	0.28	21.5	22	42	34
zmus_z1_21	3	0.32	20	20	31	90
zmus_z1_119	4	0.25	21	21	62	60
zmus_z1_166	3	0.32	22	21.5	51	80
zmus_z1_217	4	0.25	23	22.5	70	58

Table 3.1: Parameters used in $^{3D}Barolo$'s task ELLPROF in order to obtain surface brightness profiles from the Hα intensity maps.

3.2 Galpynamics

To reproduce the observed rotation curves, we must calculate the contributions of the various mass components. Galpynamics [2] is a Python package developed by G. Iorio and is specifically designed to compute and evaluate galactic potentials, circular speeds, and density distributions. Galpynamics' ability to construct the potential for various matter distributions, such as (poly-)exponential discs, makes it an ideal tool to use in this work.

Multiple Galpynamics functions were implemented to model stellar and gaseous discs of the galaxies in our sample. Galpynamics takes as input a mass density profile specified by the user and computes the potential and the circular speed of the given distribution. This mass distribution can be either a thick or a thin (poly-)exponential disc.

3.3 MCMC modelling

To fit the observed rotation curves, a Python routine written by Pavel Mancera Piña was used. The script is based on a Markov chain Monte Carlo (MCMC) approach, using Emcee in Python. Emcee is a Python implementation of the affine-invariant MCMC Ensemble sampler proposed by Foreman-Mackey et al. 2013.

Initially, the script was written to reconstruct rotation curves of galaxies $z = 0$. It uses Galpynamics to compute the circular speeds of the stellar and gaseous disc and compares these to the observed rotational velocity to fit and constrain a NFW halo. The ultimate aim of the Python routine is to return a value for the mass of the dark matter halo (M_{200}, see Section 1.4).

For this project, the script was modified to evaluate galaxies at $z \sim 1$. Originally, the MCMC routine was based on one free parameter, the mass of the dark matter halo. By implementing a second parameter, we let the MCMC return best estimates for both dark matter halo and gas mass.

To save computational time, the script takes an initial guess for M_{200}. This guess is made using a linear model for the SHMR (Eq. 1.9), with parameters $\log f_0 = -5.3^{+0.7}_{-0.7}$ and $\alpha = 0.35^{+0.07}_{-0.07}$, at $z = 0$ (Posti et al. 2019). This relation is given for galaxies at redshift 0, though since its function is purely to give an initial estimate, it is left unchanged. A relation that does demand modification is the concentration-mass-redshift relation (Eq. 1.8). The parameters in this relation were changed to the corresponding values at redshift 1 (see Section 1.4.2).

The Python routine calculates the three mass contributions of the galaxy: the stellar disc, the gaseous disc, and the dark matter halo. We will treat them separately in the following sections.

[2] https://github.com/giulianoiorio/galpynamics

3.3.1 Contribution of the stellar disc

First, we consider the stellar component. The script takes the stellar mass of each galaxy, as listed in Table 2.1. Stellar discs are often fitted using an exponential form. However, upon inspection stellar surface brightness profiles of some of our galaxies proved to be poorly fitted using an exponential profile. To model the variety of surface brightness profiles, we decided upon fitting a fourth order poly-exponential function. The poly-exponential function, a combination between an exponential and polynomial, is given by:

$$\Sigma(R) = \Sigma_0 \left(1 + C_1 R + C_2 R^2 + C_3 R^3 + C_4 R^4\right) exp\left(-\frac{R}{R_\Sigma}\right), \tag{3.1}$$

where Σ_0 denotes the central surface density, R_Σ is the scale radius and C_i are the polynomial coefficients (Bacchini et al. 2019).

For the stellar component, the poly-exponential function can be directly fitted to the surface brightness profile, as the surface brightness is proportional to the surface density. Once a poly-exponential disc has been constructed, we can calculate its circular speed using Galpynamics and obtain the stellar contribution to the rotation curve.

3.3.2 Contribution of the gaseous disc

Contrary to the stellar disc, we are not in possession of a pre-determined value for the mass of the gas. As mentioned in our introduction, with current instruments galaxies at $z \sim 1$ cannot be observed in neutral hydrogen. Even though galaxies at $z \sim 1$ can be observed in CO, tracing molecular gas, these observational data were not available for our galaxy sample. As a solution, we used Hα intensity maps to trace the shape of the gas disc. Subsequently, we constrained the total mass of the disc using the MCMC and a flat prior with boundaries determined by scaling relations.

To start, the Hα intensity maps of the galaxies in our sample were used. Assuming fully ionized gas, the emissivity of the Hα recombination lines is proportional to the density of the electrons times the density of the protons. This causes the surface brightness profiles to be proportional to the mass density squared. By taking the square root of the surface brightness profile, we derive profiles that have direct proportionality with the mass density of the galaxies in our sample. However, we still need to determine the normalization, as we see below.

Disc galaxies have a mass density profile which can be well described by an exponential function of the form:

$$\Sigma(R) = \Sigma_0 exp\left(-\frac{R}{R_{\rm gas}}\right), \tag{3.2}$$

where Σ_0 is the central surface density and $R_{\rm gas}$ the scale radius. We fit this exponential function to the mass density profiles of our galaxy sample, Galpynamics then uses the resulting profiles to define thin exponential gaseous discs and calculates their circular speeds.

After this, we employ two different scaling relations to estimate the gas mass in molecular and neutral hydrogen in our galaxy sample. Scaling relations describe observed trends between the physical properties of galaxies. These are important since they help us to better understand the physics of galactic processes. Additionally, well-established scaling relations can be used statistically to infer information about galactic properties, which cannot be directly obtained from observations.

Firstly, we consider the mass of the neutral hydrogen gas. Zhang et al. 2020 proposed a photometric estimator of the HI gas-to-stellar mass ratio ($M_{\rm HI}/M_*$) at $z \sim 1$. This scaling relation relies on the assumption that the correlation between $M_{\rm HI}/M_*$, the $NUV - r$ color and galactic size in the local Universe applies also at $z \sim 1$. The estimator was calibrated using a sample of 660 galaxies in the local Universe to a sample of ∼7000 galaxies in the DEEP2 survey with $0.75 < z < 1.4$ (Davis et al. 2003). The local ($z = 0$) galaxies used for calibration have been observed in HI and therefore have real observations available. Figure 3.2 shows the relation used in this work in the middle panel, given by

$$\log \frac{M_{HI}}{M_*} = 8.24 - 0.82 \log \frac{M_*}{M_\odot}, \tag{3.3}$$

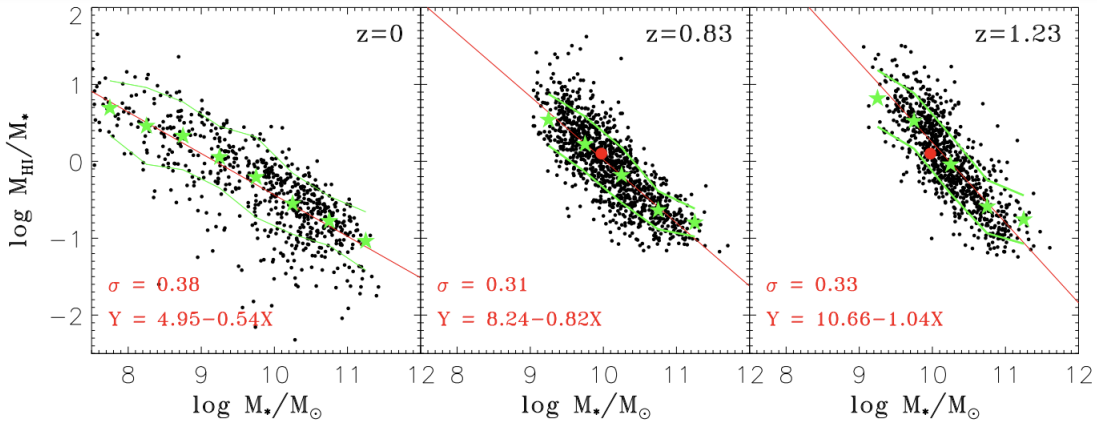

Figure 3.2: The HI-to-stellar mass ratio (M_{HI}/M_*) as a function of stellar mass at different redshifts. The black dots denote the calibrating galaxies. The left panel shows the calibrating sample at $z \sim 0$, the middle and right panels show the DEEP2 galaxies at $z > 0$. The red lines show the best fitting linear relation. The green stars and lines show the median and 1σ scatter for a number of stellar mass bins. The mean measurements of galaxies at $z \sim 1$ by Chowdhury et al. 2020 are shown as red dots. Figure adapted from Zhang et al. 2020.

The second scaling relation used to determine the gas contribution to the rotation curve, is a relation that determines the molecular gas fraction $M_{\rm mol}/M_*$ as a function of redshift. Geach et al. 2011 found a relation for a gas fraction increasing with redshift, roughly described by:

$$\frac{M_{mol}}{M_*} \sim 0.1 \cdot (1+z)^2. \tag{3.4}$$

Carilli and Walter 2013 showed good agreement with this relation by plotting a compilation of the latest measurements of molecular gas fractions in massive galaxies. Figure 3.3 displays their results.

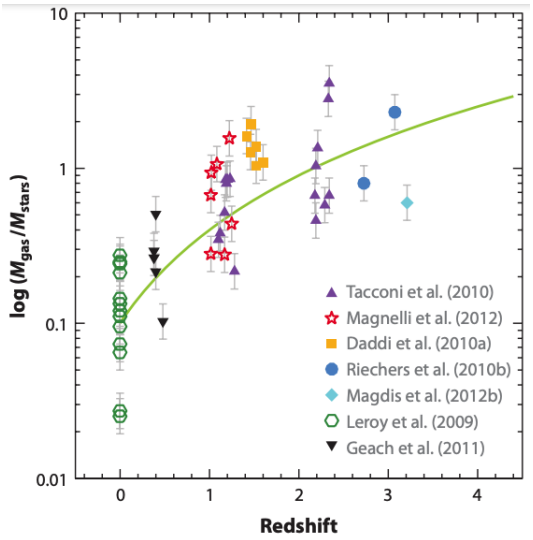

Figure 3.3: Ratio of molecular hydrogen gas-to-stellar mass $= M_{\rm mol}/M_*$ for various galaxy samples, the curve follows $M_{\rm mol}/M_* = 0.1 * (1+z)^2$ (Geach et al. 2011). Figure taken from Carilli and Walter 2013.

After estimating the mass of the neutral and molecular hydrogen using the two scaling relations, we define a prior such that the MCMC looks for masses between the minimum among $M_{\rm mol}$ and $M_{\rm HI}$, and ten times their sum. This prior is flat and serves purely to speed up the code by constraining the gas mass between reasonable limits.

3.3.3 Contribution of the dark matter halo

After the stellar and preliminary gas contributions to the total rotation curve have been established, the fiducial masses of the gaseous disc and the dark matter halo are obtained.

Starting with the halo mass we obtained earlier from the SHMR, we define a prior that is flat from 0.01 until 100 times this initial guess. In this range, our code searches for the dark matter halo that minimizes the residuals. As discussed earlier, a dark matter halo has two main parameters, the concentration, and the virial mass. By assuming our halo to follow the concentration-mass-redshift relation, we are left with one free parameter to fit a NFW profile, the virial mass (M_{200}).

The code takes a halo mass and defines a NFW profile, the velocity of the NFW profile is calculated according to Equation 1.4.1. Meanwhile, the code also takes a gas mass and normalizes the previously derived circular speed of the gas. Finally, the velocities of the stellar, gas, and dark matter halo components are added according to Equation 1.4, to create the total contribution to the rotation curve. The algorithm then compares the modelled rotation curve with the observed version and computes the residuals. Thereafter, it proceeds to the next masses.

For each combination of gas and dark matter halo masses within the specified priors, the MCMC looks for the best fit. The idea is that ultimately the MCMC returns the combination of masses that produce the lowest residuals. The values of the gas and dark matter mass for which the residuals are minimized are then assumed as the fiducial masses. The masses derived by the MCMC modelling are presented and discussed in the following Chapter.

Chapter 4

Results and discussion

The rotation curve decomposition and posterior probability distributions of the two free parameters of a representative galaxy *zcos_z*1_692 of our sample are shown in Figure 4.1. Similar plots for the remaining galaxies in our sample can be found in Appendix A. The left panels show the decomposed rotation curves. The observational data is represented by the grey band, the original points of the rotation curves from TFM16 are seen as grey dots. The inner point of the rotation curve is the most uncertain, therefore the error in this point is represented by the spectral resolution. This is the line broadening introduced by the instrument and has a value of $\sigma_{\text{instr}} \sim 30$ km/s. The stellar, gas, and dark matter halo components are displayed by the yellow, blue, and black line, respectively. The sum of these mass components is shown by the red line.

The right panel of Figure 4.1 shows the corresponding posterior probability distributions of the free parameters of the fit, returned by the MCMC. The best estimates for the dark matter halo mass (M_{200}) and gas mass (M_{gas}) are displayed in the Figure and listed in Table 4.1.

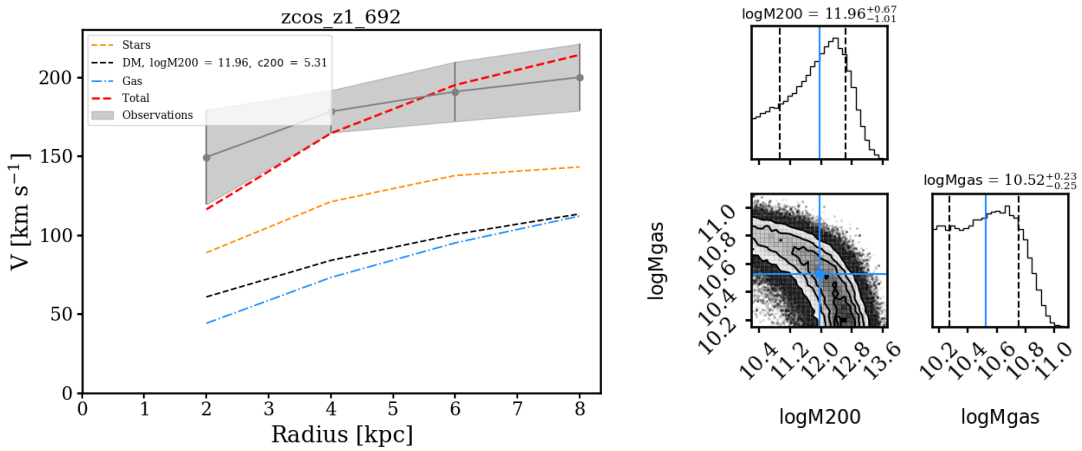

Figure 4.1: Left Figure: Rotation curve decomposition plot of the galaxy *zcos_z*1_692. The yellow, blue and black lines showing the stellar, gas, and dark matter halo contributions respectively. The red line denotes the total of the previously mentioned components and the grey band displays the observed rotation curve from TFM16. Right Figure: Corner plot displaying the posterior probability distributions of the free parameters of the fit.

Figure 1.1 in our introduction displays a typical rotation curve. As can be seen in this Figure, we expect the dynamics in the inner regions of the rotation curves to be dominated by the luminous matter. In addition to this, the dark matter contribution is expected to increase and become more important as we move outwards from the center. We notice that the baryonic contributions in some of our galaxies poorly reproduce the inner regions of the rotation curves. When the baryonic contributions are small, the MCMC attempts to minimize the residuals by overcompensating the dark matter contribution. Nevertheless, even with very massive halos, we did not manage to reproduce the inner part of the rotation curves of some of the galaxies in our sample.

A good fit is determined by how well the red line in the left panel follows the observational data. To quantify the goodness of the fits, we computed the reduced chi-squares (χ^2). The reduced chi-squares of our fits are listed in Table 4.1 and range from 0.66 to 15.80. The closer the χ^2 value is to one, the better we conclude the fit is. As can be seen in the rotation curve decomposition plots in Appendix A, for some galaxies we find a relatively good fit, whereas for others we did not manage to reconstruct the observed rotation curve properly.

As can be seen in the left panel of Figure 4.1, the observed rotation curve of this galaxy was well reconstructed by the different mass components ($\chi^2 = 1.39$). In this galaxy, the potential in the inner region is dominated by the stellar disc. This is not the case for all the galaxies: some of the galaxies show potentials dominated by the dark matter halos in the inner regions. The contribution of the gaseous disc is subdominant, which is the case for all galaxies in our sample. The shallow shapes of the gas components may have been caused by the low resolution of the data, as we will discuss shortly. The posterior probability distributions of M_{200} and $M_{\rm gas}$ in the right panel of Figure 4.1, show dissimilar shapes. The shape of the posterior of M_{200} shows a clear peak compared to the flatter shape of the posterior of $M_{\rm gas}$. This is a general rule we observe in all galaxies in our sample (see Appendix A), the absence of peaks in the $M_{\rm gas}$ posteriors, indicates that the mass of the gas was not well constrained.

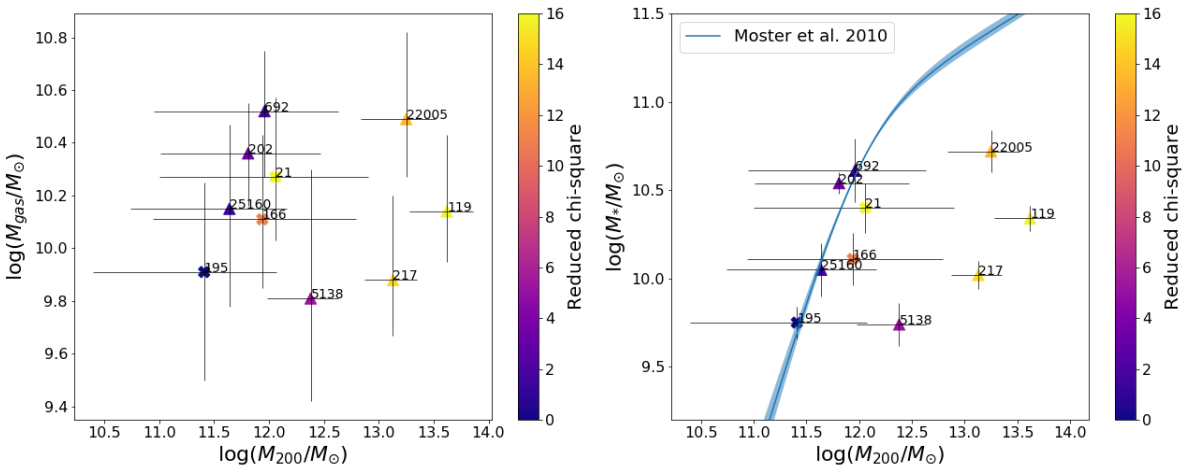

Figure 4.2: Left Figure: mass of the gaseous discs set out against the mass of the dark matter halos. Right Figure: mass of the stellar discs set out against the mass of the dark matter halos. The color gradient shows the computed χ^2's. Galaxies having rotation curves with values at four and three radii are marked with triangles and crosses, respectively. Abbreviations of the names of the corresponding galaxies are listed with the markers. The blue curve shows the stellar-to-halo mass relation at $z \sim 1$ and its uncertainty proposed by Moster et al. 2010, with parameters from Girelli et al. 2020.

Figures 4.2 and 4.4 are graphical representations of the best estimates for the dark matter halo and gas masses, computed using the MCMC. In these Figures, the goodness of the fits of the individual galaxies is represented by a color gradient ranging from dark blue to yellow, denoting a relatively good and bad fit, respectively.

In Figure 4.4 and in the right panel of Figure 4.2, the SHMR at $z \sim 1$ mentioned in our Introduction (Eq.1.10) is shown by the blue band. As can be seen in these Figures, well-fitted galaxies tend to appear closer to the plotted SHMR. We emphasize that this SHMR is not unique, there exist different functions and parameterizations for the SHMR, and scatter around them has been reported. From the SHMR, we expect galaxies with stellar masses like the ones in our sample to live in dark matter halos of roughly $10^{12}\ M_\odot$. However, some of the decompositions return dark matter halos masses larger than $10^{13}\ M_\odot$. Since dark matter halos this massive are highly unrealistic for the corresponding stellar masses, we conclude these fits are not reliable, which is confirmed by their large χ^2 values.

4.1 Reliability of the fits

Multiple causes may have led to the poorly reconstructed rotation curves, some of the most probable causes will be discussed now.

To start, we stress that our method is based on various assumptions and generalizations which may have caused inaccuracy. Examples include invalid choices of fitting functions to determine the shapes of the mass components and letting our galaxies follow precisely the concentration-mass redshift relation.

Secondly, as mentioned in Chapter 2, the stellar masses of the galaxies used in this work were taken from TFM16, but have been derived by different sources. These stellar masses have associated uncertainties, different values for them have been reported, such as in Stott et al. 2016. For some galaxies in our sample, the fit may have been better if the stellar contribution was more dominant. Nevertheless, the stellar masses reported in Stott et al. 2016, are not systematically larger than the stellar masses used in this work, so we dare not draw any strong conclusions from this.

Likely, the most important cause of error in our results is the low resolution of the observations. We make use of Hα emission-line data to trace the gas mass distribution in our galaxies. The spatial resolution of these observations is typically $\sim 0.5" - 0.6"$, causing there to be very few independent resolution elements across the discs (which have radii of $\sim 1"$). Consequently, the density profiles used to determine the gas contributions to the rotation curves are flattened out. Figures A.2 in the Appendix show the surface brightness profiles of the stellar and gaseous discs of the galaxies in our sample, Figure 4.3 shows these for galaxy *zcos_z*1_692. The plotted lines are the (poly-)exponential fits used to trace the shape of the corresponding discs. Where the gaseous profiles in reality could have been intrinsically steep, they appear flattened out by the resolution. As a consequence, the contributions of the gaseous discs to the inner parts of the rotation curves are small.

The rotation curves obtained from TFM16 are derived from the same Hα emission-line data. They consist of values at three or four radii, but these are not independent. As a consequence of this, as described in TFM16, we can expect the rotational velocities in the inner points of the rotation curves to be overestimated. The combination of these two effects may have caused us to end up with rotation curves that cannot be reproduced with baryonic matter in the inner regions.

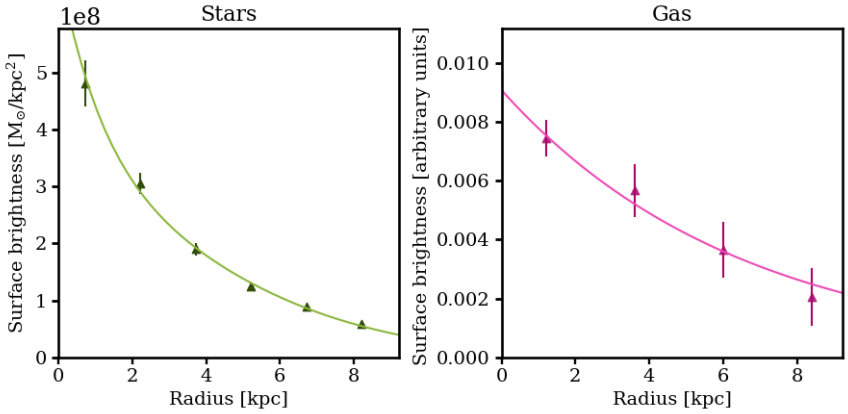

Figure 4.3: Left panel: stellar surface brightness profile of the galaxy *zcos_z*1_692 from Marasco et al. 2019, fitted with a poly-exponential function. Right panel: Hα surface brightness profile of the galaxy *zcos_z*1_692, obtained in this work and fitted with an exponential function.

Name	**Abbrev**	$\log M_*/M_\odot$	$\log M_{\rm gas}/M_\odot$	$\log M_{200}/M_\odot$	χ^2	**RE**	$\Sigma_{0,\rm gas}$ $M_\odot/\rm kpc^2$	$\mathbf{R}_{\rm gas}$ kpc
gs3_22005†	22005	10.72 ±0.12	$10.49^{+0.33}_{-0.22}$	$13.25^{+0.27}_{-0.41}$	13.55	4	1.32e8	37.41
hiz_z1_195	195	9.75 ±0.09	$9.91^{+0.34}_{-0.41}$	$11.41^{+0.66}_{-1.01}$	0.66	3	3.52e7	10.53
u3_5138†	5138	9.74 ±0.12	$9.81^{+0.49}_{-0.39}$	$12.38^{+0.25}_{-0.40}$	5.26	4	3.98e7	21.37
u3_25160†	25160	10.05 ±0.15	$10.15^{+0.32}_{-0.37}$	$11.64^{+0.52}_{-0.90}$	1.37	4	9.44e7	13.18
zcos_z1_202	202	10.54 ±0.06	$10.36^{+0.19}_{-0.20}$	$11.91^{+0.66}_{-1.00}$	3.44	4	2.44e8	11.39
zcos_z1_692	692	10.61 ±0.18	$10.52^{+0.23}_{-0.25}$	$11.96^{+0.67}_{-1.01}$	1.39	4	2.06e8	12.06
zmus_z1_21	21	10.40 ±0.14	$10.27^{+0.30}_{-0.24}$	$12.06^{+0.84}_{-1.08}$	15.48	3	1.61e8	20.81
zmus_z1_119	119	10.34 ±0.07	$10.14^{+0.29}_{-0.19}$	$13.62^{+0.24}_{-0.34}$	15.80	4	1.11e8	14.00
zmus_z1_166	166	10.11 ±0.15	$10.11^{+0.32}_{-0.26}$	$11.95^{+0.85}_{-1.00}$	10.87	3	1.18e8	12.23
zmus_z1_217	217	10.02 ±0.08	$9.88^{+0.32}_{-0.21}$	$13.13^{+0.22}_{-0.26}$	14.84	4	5.37e7	20.07

Table 4.1: From left to right: names adopted in the main survey (KMOS3*D*/KROSS), abbreviations used in the Figures in this Chapter, stellar masses and corresponding uncertainties from TFM16, gas masses and their 68% confidence intervals, dark matter halo masses and their 68% confidence intervals, computed reduced chi-squares of the fits, number of radii in the rotation curves, central surface density of the gaseous disc, scale length of the gaseous disc. Galaxies belonging to the KMOS3*D* survey are marked (†), the remaining galaxies belong to the KROSS survey.

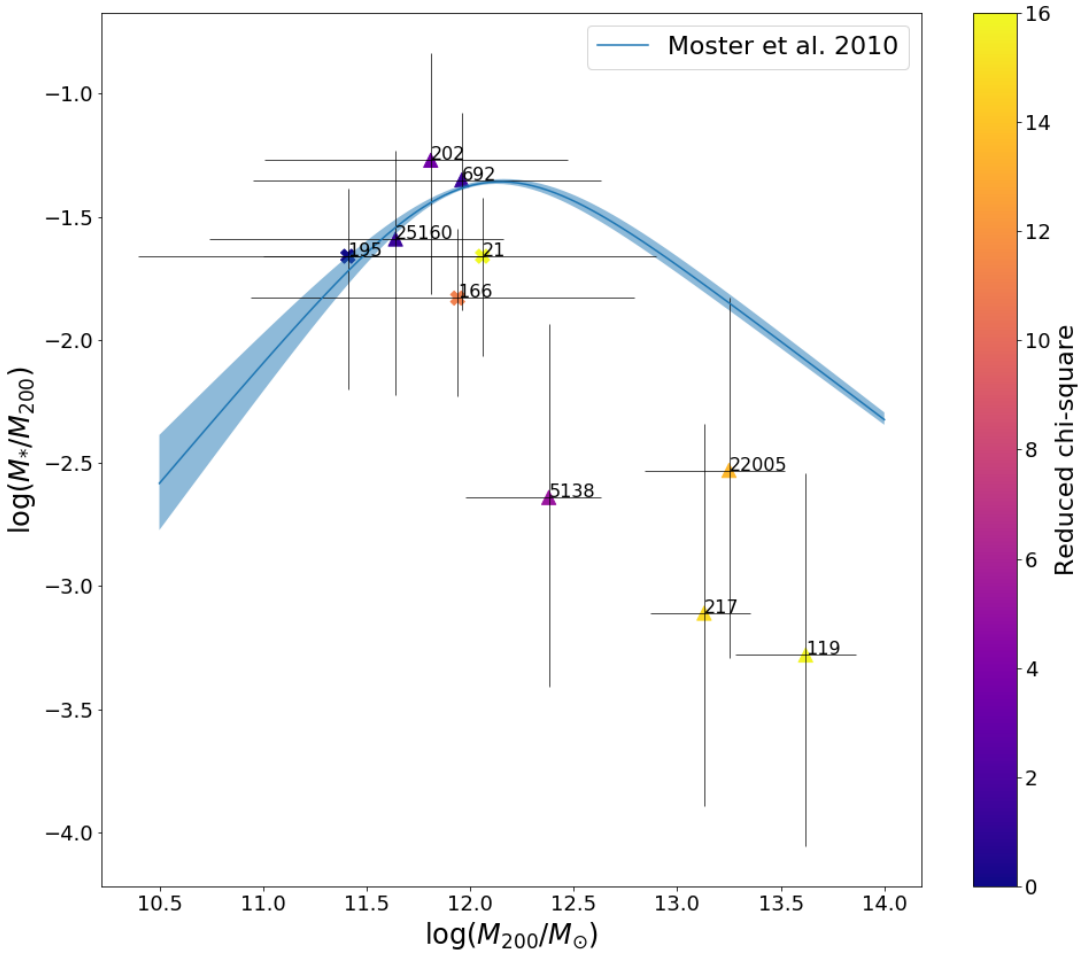

Figure 4.4: Visualisation of the stellar-to-halo mass relation at $z \sim 1$. The color gradient shows the computed χ^2's. Galaxies having rotation curves with values at four and three radii are marked with triangles and crosses, respectively. Abbreviations of the names of the corresponding galaxies are listed with the markers. The blue curve shows the stellar-to-halo mass relation and its uncertainty proposed by Moster et al. 2010, with parameters from Girelli et al. 2020.

Chapter 5

Conclusions

Studies have shown that rotational velocities in the outer edges of disc galaxies generally do not decline in accordance with the Keplerian fall, which is expected on the basis of the observed distribution of luminous matter. Instead, rotational velocities of disc galaxies tend to stay constant out to the outermost radii. In other words, measured velocities on the outskirts of galaxies are too large to be solely caused by the visible amount of matter. The dynamically inferred missing matter, in the form of a large non-baryonic dark matter halo, provides a solution to this supposed discrepancy.

In this project, we performed rotation curve decomposition of a sample of galaxies at $z \sim 1$. Based on the knowledge that the rotational velocity of a galaxy is a direct result of its galactic potential, we attempted to reconstruct observed rotation curves by considering the three main mass components: the stellar disc, the gaseous disc and the dark matter halo.

We made use of previously determined stellar masses and stellar surface brightness profiles to determine the shape of the disc. The mass of the gas and dark matter halo were determined using a MCMC routine, we adopted flat priors for both the dark matter halo and the gaseous disc. We traced the shape of the gaseous disc with the use of Hα intensity maps. For the shape of the dark matter halo, we assumed a NFW profile. Assuming the halo follows the concentration-mass relation, we took the virial mass as the only free parameter for the dark matter halo. The observed rotational velocities were then used in the MCMC to return the best estimates for the gas and dark matter masses.

Reduced chi-square values of the fits following from the rotation curve decomposition range from 0.45 to 15.76. We quantify the goodness of the fits by how close the reduced χ^2 value is to 1. In Figure 4.4 it can be seen that when the fit is relatively good, the galaxies appear closer to the SHMR determined at $z = 1$ by other authors with independent techniques. This means that the dark matter halo masses we derived for the well-fitting galaxies are close to the expected values. This indicates that rotation curve decomposition is a valid method to use for reconstructing dark matter halos at $z \sim 1$, in cases in which the fit is good and hence the reduced χ^2 is close to 1.

We discussed potential causes of errors in our fitting strategy. Firstly, errors may have been caused by employment of inaccurate fitting functions and assumptions. Secondly, the uncertainty of the stellar masses used in this work may have caused inaccurate stellar contributions to the rotation curves. Most importantly, the low-resolution of the observational data has likely flattened out the density profiles of the gaseous components, which were used to derive the gas contribution to the observed rotation curves. Meanwhile, the low resolution of the data also may have raised the inner points of the observed rotation curves. These two effects combined cause the rotation curves to be poorly reproduced with baryonic matter in the inner regions. In future studies, one could try to resolve this problem by deconvolving the observed gas profiles, or by making use of observations at higher spatial resolution.

Bibliography

Allen, R. J. et al. (Sept. 2011). *GIPSY: Groningen Image Processing System*. ascl: 1109.018.

Bacchini, Cecilia et al. (Feb. 2019). "Volumetric star formation laws of disc galaxies". In: 622, A64, A64. DOI: 10.1051/0004-6361/201834382. arXiv: 1810.03616 [astro-ph.GA].

Binney, James and Scott Tremaine (2008). *Galactic Dynamics: Second Edition*.

Blumenthal, G. R. et al. (Oct. 1984). "Formation of galaxies and large-scale structure with cold dark matter." In: 311, pp. 517–525. DOI: 10.1038/311517a0.

Bosma, A. (Jan. 1978). "The distribution and kinematics of neutral hydrogen in spiral galaxies of various morphological types". PhD thesis. -.

Bullock, J. S. et al. (July 2001). "A Universal Angular Momentum Profile for Galactic Halos". In: 555.1, pp. 240–257. DOI: 10.1086/321477. arXiv: astro-ph/0011001 [astro-ph].

Carilli, C. L. and F. Walter (Aug. 2013). "Cool Gas in High-Redshift Galaxies". In: 51.1, pp. 105–161. DOI: 10.1146/annurev-astro-082812-140953. arXiv: 1301.0371 [astro-ph.CO].

Chowdhury, Aditya et al. (Oct. 2020). "H I 21-centimetre emission from an ensemble of galaxies at an average redshift of one". In: 586.7829, pp. 369–372. DOI: 10.1038/s41586-020-2794-7. arXiv: 2010.06617 [astro-ph.GA].

Cimatti, Andrea, Filippo Fraternali, and Carlo Nipoti (2020). *Introduction to Galaxy Formation, From Primordial Gas to Present-Day Galaxies*. DOI: 10.1017/9781316471180. URL: https://www.cambridge.org/9781107134768.

Colless, Matthew and Andrew M. Dunn (Feb. 1996). "Structure and Dynamics of the Coma Cluster". In: 458, p. 435. DOI: 10.1086/176827. arXiv: astro-ph/9508070 [astro-ph].

Davis, Marc et al. (Feb. 2003). "Science Objectives and Early Results of the DEEP2 Redshift Survey". In: *Discoveries and Research Prospects from 6- to 10-Meter-Class Telescopes II*. Ed. by Puragra Guhathakurta. Vol. 4834. Society of Photo-Optical Instrumentation Engineers (SPIE) Conference Series, pp. 161–172. DOI: 10.1117/12.457897. arXiv: astro-ph/0209419 [astro-ph].

Di Teodoro, E. M. and F. Fraternali (Aug. 2015). "^{3D} BAROLO: a new 3D algorithm to derive rotation curves of galaxies". In: 451.3, pp. 3021–3033. DOI: 10.1093/mnras/stv1213. arXiv: 1505.07834 [astro-ph.GA].

Di Teodoro, E. M., F. Fraternali, and S. H. Miller (Oct. 2016). "Flat rotation curves and low velocity dispersions in KMOS star-forming galaxies at z $\sim$1". In: 594, A77, A77. DOI: 10.1051/0004-6361/201628315. arXiv: 1602.04942 [astro-ph.GA].

Doroshkevich, Andrei G., Vladimir N. Lukash, and Elena V. Mikheeva (Jan. 2012). "A solution to the problems of cusps and rotation curves in dark matter halos in the cosmological standard model". In: *Physics Uspekhi* 55.1, pp. 3–17. DOI: 10.3367/UFNe.0182.201201a.0003. arXiv: 1209.0388 [astro-ph.CO].

Dutton, Aaron A. and Andrea V. Macciò (July 2014). "Cold dark matter haloes in the Planck era: evolution of structural parameters for Einasto and NFW profiles". In: 441.4, pp. 3359–3374. DOI: 10.1093/mnras/stu742. arXiv: 1402.7073 [astro-ph.CO].

Einasto, J. and U. Haud (Oct. 1989). "Galactic models with massive corona. I - Method. II - Galaxy". In: 223.1-2, pp. 89–106.

Fall, S. M. and G. Efstathiou (Oct. 1980). "Formation and rotation of disc galaxies with haloes." In: 193, pp. 189–206. DOI: 10.1093/mnras/193.2.189.

Faulkner, J. and R. L. Gilliland (Dec. 1985). "Weakly interacting, massive particles and the solar neutrino flux". In: 299, pp. 994–1000. DOI: 10.1086/163766.

Foreman-Mackey, Daniel et al. (Mar. 2013). "emcee: The MCMC Hammer". In: 125.925, p. 306. DOI: 10.1086/670067. arXiv: 1202.3665 [astro-ph.IM].

Förster Schreiber, N. M. et al. (Dec. 2009). "The SINS Survey: SINFONI Integral Field Spectroscopy of z ∼2 Star-forming Galaxies". In: 706.2, pp. 1364–1428. DOI: 10.1088/0004-637X/706/2/1364. arXiv: 0903.1872 [astro-ph.CO].

Freese, K. (Jan. 2009). "Review of Observational Evidence for Dark Matter in the Universe and in upcoming searches for Dark Stars". In: *EAS Publications Series*. Ed. by E. Pécontal et al. Vol. 36. EAS Publications Series, pp. 113–126. DOI: 10.1051/eas/0936016. arXiv: 0812.4005 [astro-ph].

Geach, J. et al. (July 2011). "The evolution of the molecular gas fraction of star-forming galaxies". In: *Galaxy Formation*, p. 43.

Girelli, G. et al. (Feb. 2020). "The stellar-to-halo mass relation over the past 12 Gyr. I. Standard ΛCDM model". In: 634, A135, A135. DOI: 10.1051/0004-6361/201936329. arXiv: 2001.02230 [astro-ph.CO].

Grogin, Norman A. et al. (Dec. 2011). "CANDELS: The Cosmic Assembly Near-infrared Deep Extragalactic Legacy Survey". In: 197.2, 35, p. 35. DOI: 10.1088/0067-0049/197/2/35. arXiv: 1105.3753 [astro-ph.CO].

Kirby, Emma M. et al. (Mar. 2012). "The Local Volume H I Survey: galaxy kinematics". In: 420.4, pp. 2924–2943. DOI: 10.1111/j.1365-2966.2011.20103.x. arXiv: 1202.0354 [astro-ph.CO].

Koekemoer, Anton M. et al. (Dec. 2011). "CANDELS: The Cosmic Assembly Near-infrared Deep Extragalactic Legacy Survey—The Hubble Space Telescope Observations, Imaging Data Products, and Mosaics". In: 197.2, 36, p. 36. DOI: 10.1088/0067-0049/197/2/36. arXiv: 1105.3754 [astro-ph.CO].

Kormendy, J. and K. C. Freeman (July 2004). "Scaling Laws for Dark Matter Halos in Late-Type and Dwarf Spheroidal Galaxies". In: *Dark Matter in Galaxies*. Ed. by S. Ryder et al. Vol. 220, p. 377. arXiv: astro-ph/0407321 [astro-ph].

Kriek, Mariska et al. (July 2009). "An Ultra-Deep Near-Infrared Spectrum of a Compact Quiescent Galaxy at z = 2.2". In: 700.1, pp. 221–231. DOI: 10.1088/0004-637X/700/1/221. arXiv: 0905.1692 [astro-ph.CO].

Li, Pengfei et al. (Mar. 2020). "A Comprehensive Catalog of Dark Matter Halo Models for SPARC Galaxies". In: 247.1, 31, p. 31. DOI: 10.3847/1538-4365/ab700e. arXiv: 2001.10538 [astro-ph.GA].

Ludlow, Aaron D. et al. (Apr. 2014). "The mass–concentration–redshift relation of cold dark matter haloes". In: *Monthly Notices of the Royal Astronomical Society* 441.1, pp. 378–388. ISSN: 0035-8711. DOI: 10.1093/mnras/stu483. eprint: https://academic.oup.com/mnras/article-pdf/441/1/378/2996980/stu483.pdf. URL: https://doi.org/10.1093/mnras/stu483.

Marasco, A. et al. (Jan. 2019). "The angular momentum of disc galaxies at z = 1". In: 621, L6, p. L6. DOI: 10.1051/0004-6361/201834456. arXiv: 1812.08479 [astro-ph.GA].

Moster, Benjamin P. et al. (Feb. 2010). "Constraints on the Relationship between Stellar Mass and Halo Mass at Low and High Redshift". In: 710.2, pp. 903–923. DOI: 10.1088/0004-637X/710/2/903. arXiv: 0903.4682 [astro-ph.CO].

Navarro, Julio F., Carlos S. Frenk, and Simon D. M. White (May 1996). "The Structure of Cold Dark Matter Halos". In: 462, p. 563. DOI: 10.1086/177173. arXiv: astro-ph/9508025 [astro-ph].

Neeleman, Marcel et al. (May 2020). "A cold, massive, rotating disk galaxy 1.5 billion years after the Big Bang". In: *Nature* 581, pp. 269–272. DOI: 10.1038/s41586-020-2276-y.

Planck Collaboration, N. Aghanim, et al. (Sept. 2020). "Planck 2018 results. VI. Cosmological parameters". In: 641, A6, A6. DOI: 10.1051/0004-6361/201833910. arXiv: 1807.06209 [astro-ph.CO].

Planck Collaboration, Fermi Collaboration, et al. (Oct. 2015). "Planck intermediate results. XXVIII. Interstellar gas and dust in the Chamaeleon clouds as seen by Fermi LAT and Planck". In: 582, A31, A31. DOI: 10.1051/0004-6361/201424955. arXiv: 1409.3268 [astro-ph.HE].

Posti, Lorenzo et al. (Sept. 2019). "Galaxy disc scaling relations: A tight linear galaxy-halo connection challenges abundance matching". In: 629, A59, A59. DOI: 10.1051/0004-6361/201935982. arXiv: 1909.01344 [astro-ph.GA].

Rees, M. J. and J. P. Ostriker (June 1977). "Cooling, dynamics and fragmentation of massive gas clouds: clues to the masses and radii of galaxies and clusters." In: 179, pp. 541–559. DOI: 10.1093/mnras/179.4.541.

Rizzo, F. et al. (Sept. 2020). "A dynamically cold disk galaxy in the early Universe". In: *arXiv e-prints*, arXiv:2009.01251, arXiv:2009.01251. arXiv: 2009.01251 [astro-ph.GA].

Rubin, V. C., Jr. Ford W. K., and N. Thonnard (June 1980). "Rotational properties of 21 SC galaxies with a large range of luminosities and radii, from NGC 4605 (R=4kpc) to UGC 2885 (R=122kpc)." In: 238, pp. 471–487. DOI: 10.1086/158003.

Santini, P. et al. (Mar. 2015). "Stellar Masses from the CANDELS Survey: The GOODS-South and UDS Fields". In: 801.2, 97, p. 97. DOI: 10.1088/0004-637X/801/2/97. arXiv: 1412.5180 [astro-ph.GA].

Steigman, G. et al. (Sept. 1978). "Dynamical interactions and astrophysical effects of stable heavy neutrinos." In: 83, pp. 1050–1061. DOI: 10.1086/112290.

Stott, John P. et al. (Apr. 2016). "The KMOS Redshift One Spectroscopic Survey (KROSS): dynamical properties, gas and dark matter fractions of typical z ∼ 1 star-forming galaxies". In: 457.2, pp. 1888–1904. DOI: 10.1093/mnras/stw129. arXiv: 1601.03400 [astro-ph.GA].

van Albada, T. S. and R. Sancisi (Dec. 1986). "Dark Matter in Spiral Galaxies". In: *Philosophical Transactions of the Royal Society of London Series A* 320.1556, pp. 447–464. DOI: 10.1098/rsta.1986.0128.

White, S. D. M. and M. J. Rees (May 1978). "Core condensation in heavy halos: a two-stage theory for galaxy formation and clustering." In: 183, pp. 341–358. DOI: 10.1093/mnras/183.3.341.

Wisnioski, E. et al. (Feb. 2015). "The KMOS^{3D} Survey: Design, First Results, and the Evolution of Galaxy Kinematics from 0.7 <= z <= 2.7". In: 799.2, 209, p. 209. DOI: 10.1088/0004-637X/799/2/209. arXiv: 1409.6791 [astro-ph.GA].

Zhang, Wei et al. (Nov. 2020). "A study of the HI gas fractions of galaxies at z ∼1". In: *arXiv e-prints*, arXiv:2011.04500, arXiv:2011.04500. arXiv: 2011.04500 [astro-ph.GA].

Zwicky, F. (Jan. 1933). "Die Rotverschiebung von extragalaktischen Nebeln". In: *Helvetica Physica Acta* 6, pp. 110–127.

Appendix A

Results

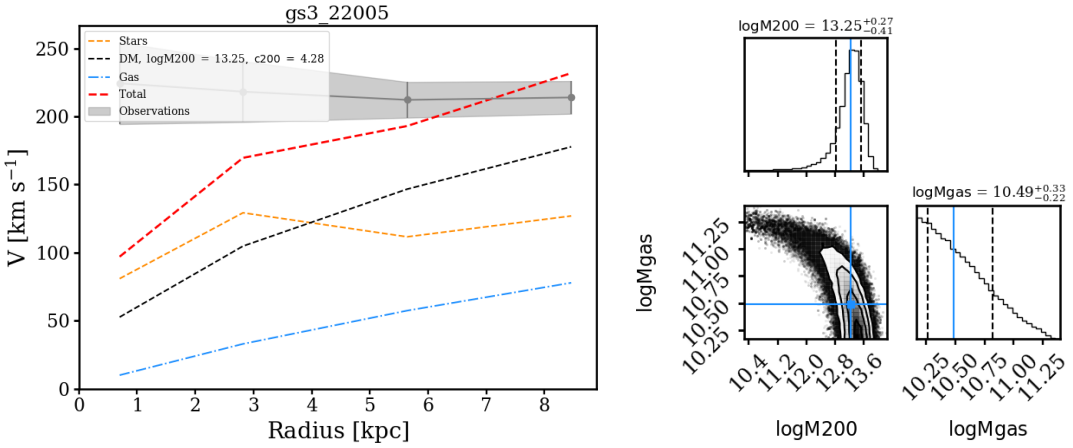

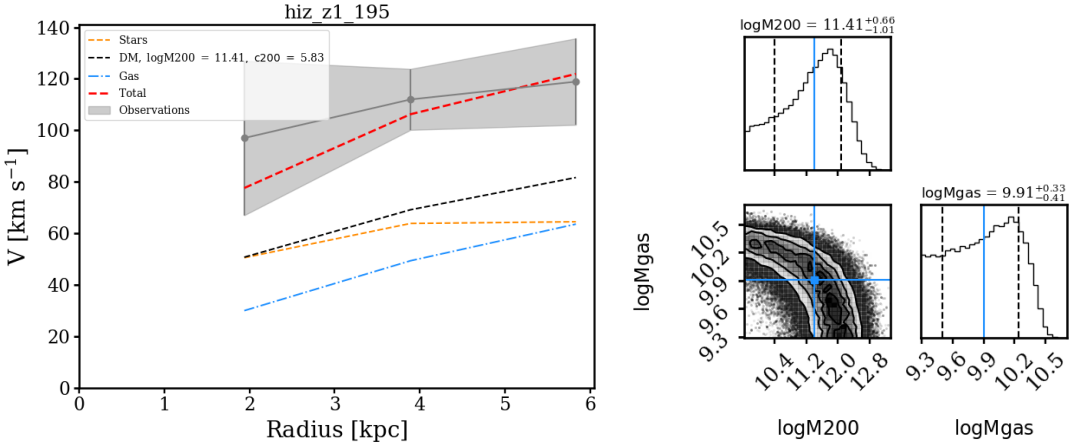

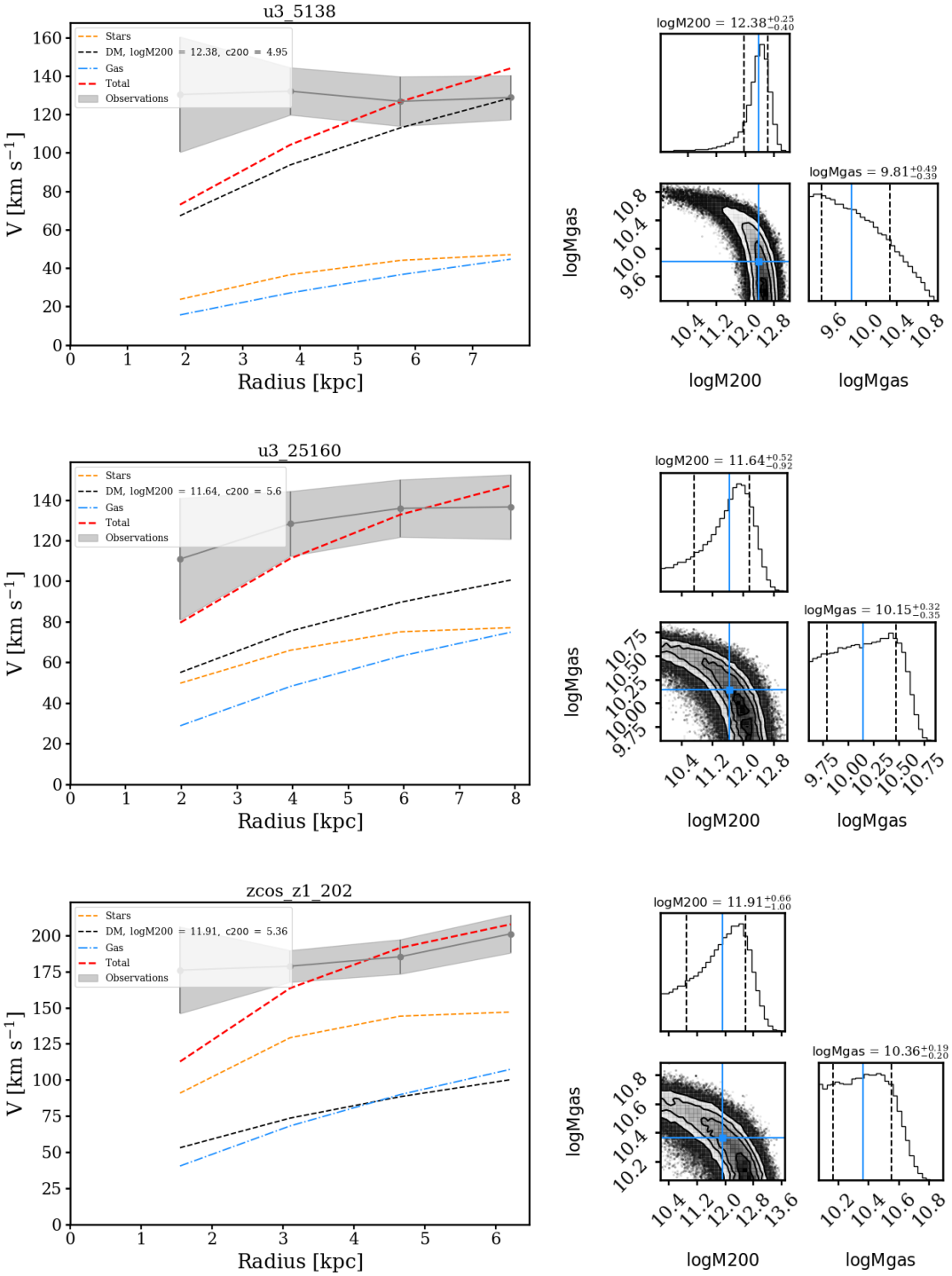
u3_5138
Stars
DM, logM200 = 12.38, c200 = 4.95
Gas
Total
Observations
V [km s^{-1}]
Radius [kpc]
logM200 = 12.38$^{+0.25}_{-0.40}$
logMgas = 9.81$^{+0.49}_{-0.39}$
logMgas
logM200
logMgas
u3_25160
Stars
DM, logM200 = 11.64, c200 = 5.6
Gas
Total
Observations
V [km s^{-1}]
Radius [kpc]
logM200 = 11.64$^{+0.52}_{-0.92}$
logMgas = 10.15$^{+0.32}_{-0.35}$
logMgas
logM200
logMgas
zcos_z1_202
Stars
DM, logM200 = 11.91, c200 = 5.36
Gas
Total
Observations
V [km s^{-1}]
Radius [kpc]
logM200 = 11.91$^{+0.66}_{-1.00}$
logMgas = 10.36$^{+0.19}_{-0.20}$
logMgas
logM200
logMgas

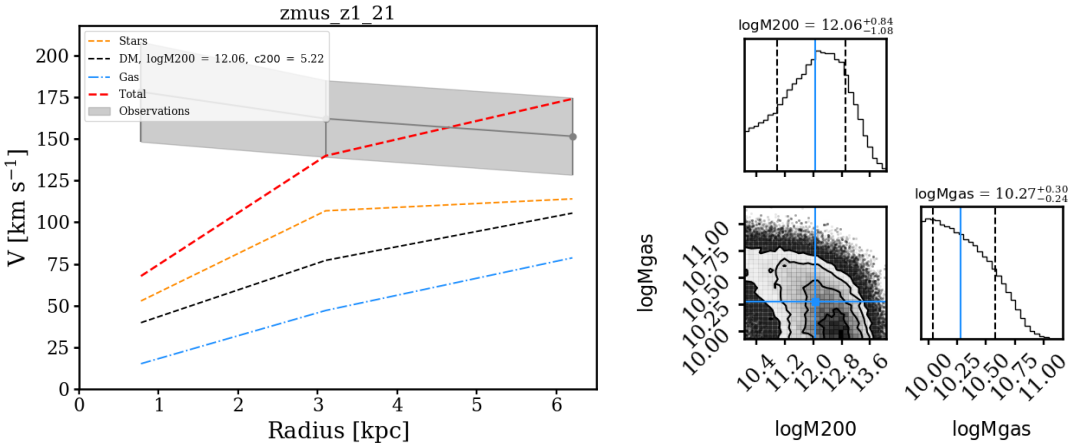
zmus_z1_21
Stars
DM, logM200 = 12.06, c200 = 5.22
Gas
Total
Observations
V [km s^{-1}]
Radius [kpc]
logM200 = $12.06^{+0.84}_{-1.08}$
logMgas = $10.27^{+0.30}_{-0.24}$
logMgas
logM200
logMgas

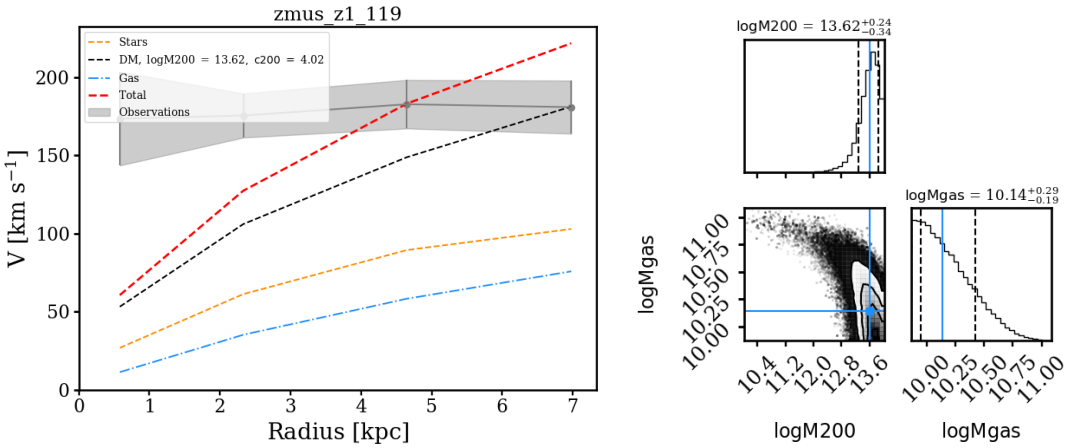
zmus_z1_119
Stars
DM, logM200 = 13.62, c200 = 4.02
Gas
Total
Observations
V [km s^{-1}]
Radius [kpc]
logM200 = $13.62^{+0.24}_{-0.34}$
logMgas = $10.14^{+0.29}_{-0.19}$
logMgas
logM200
logMgas

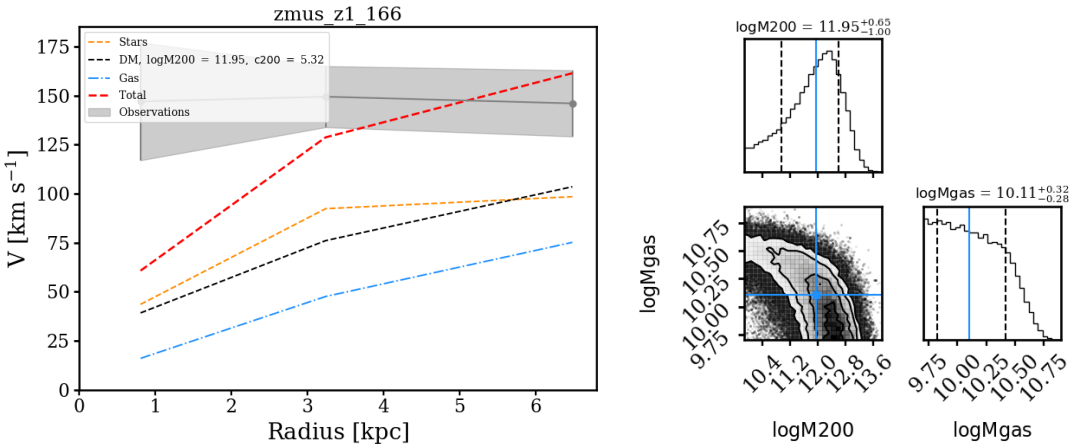
zmus_z1_166
Stars
DM, logM200 = 11.95, c200 = 5.32
Gas
Total
Observations
V [km s^{-1}]
Radius [kpc]
logM200 = $11.95^{+0.65}_{-1.00}$
logMgas = $10.11^{+0.32}_{-0.28}$
logMgas
logM200
logMgas

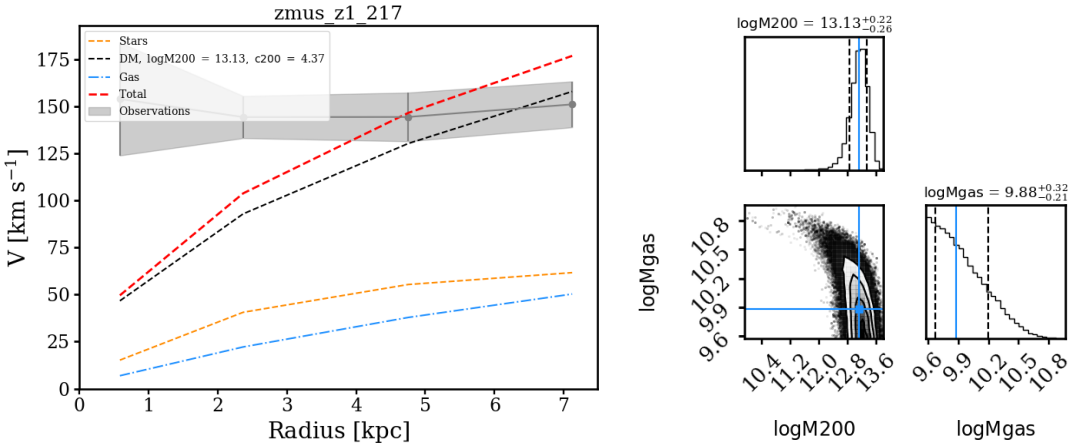

Figure A.1: Left Figures: rotation curve decomposition plots of the galaxies in our sample. The yellow, blue and black lines showing the stellar, gas and dark matter halo contributions respectively. The red lines denote the total of the previously mentioned components and the grey bands display the observed rotation curves from TFM16. Right Figures: corner plots displaying the posterior probability distributions of the free parameters of the fits.

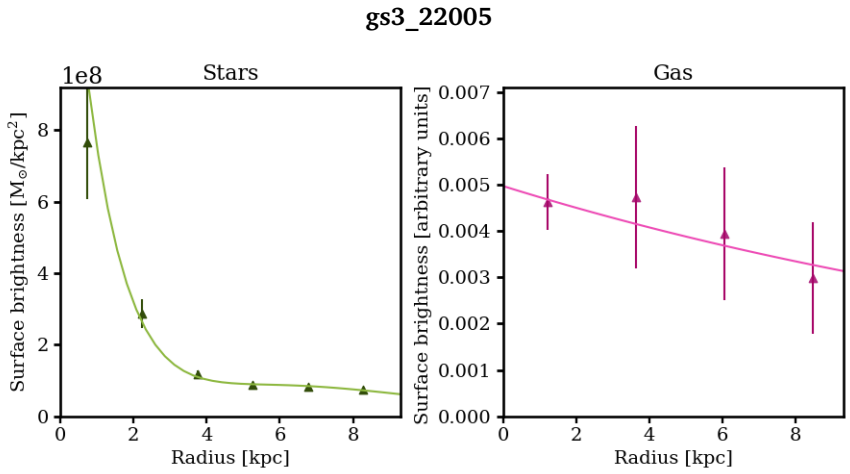

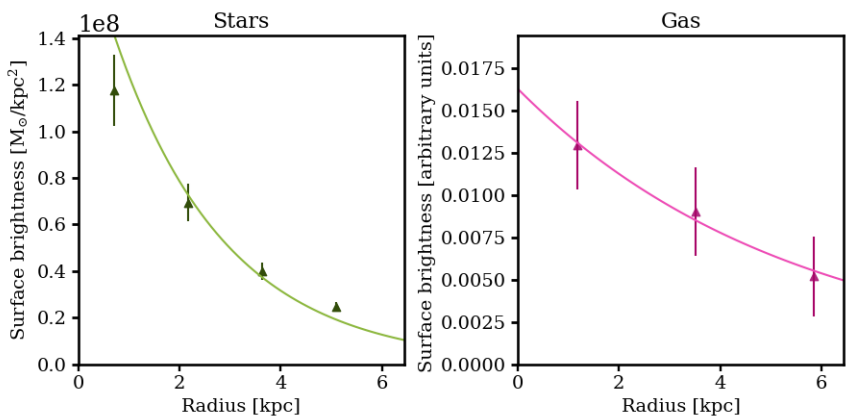

u3_5138

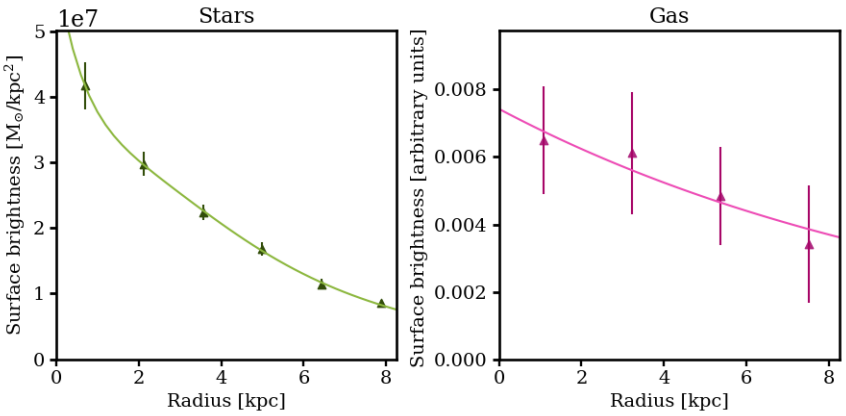

u3_25160

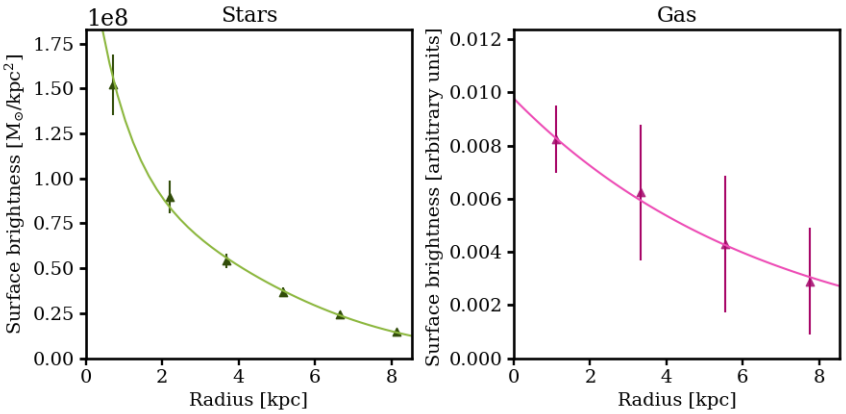

zcos_z1_202

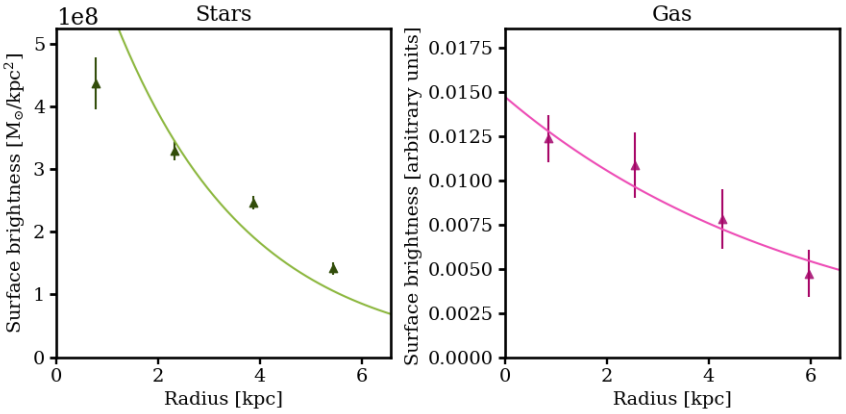

zmus_z1_21

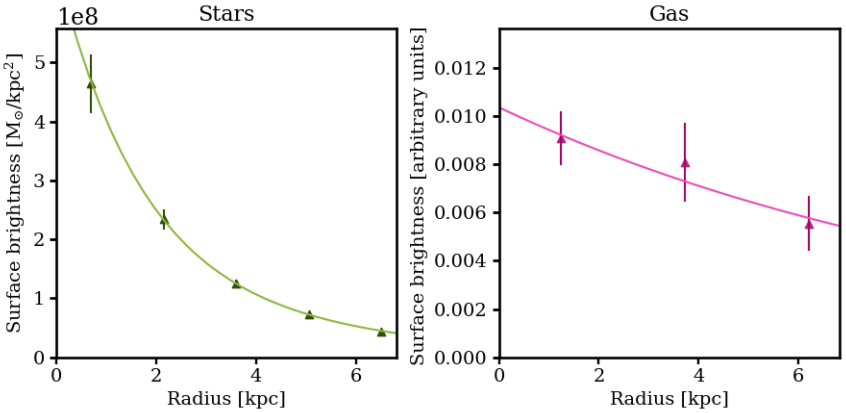

zmus_z1_119

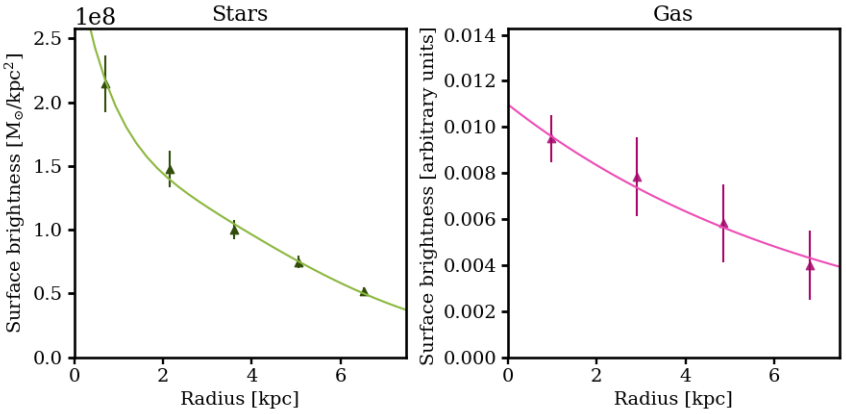

zmus_z1_166

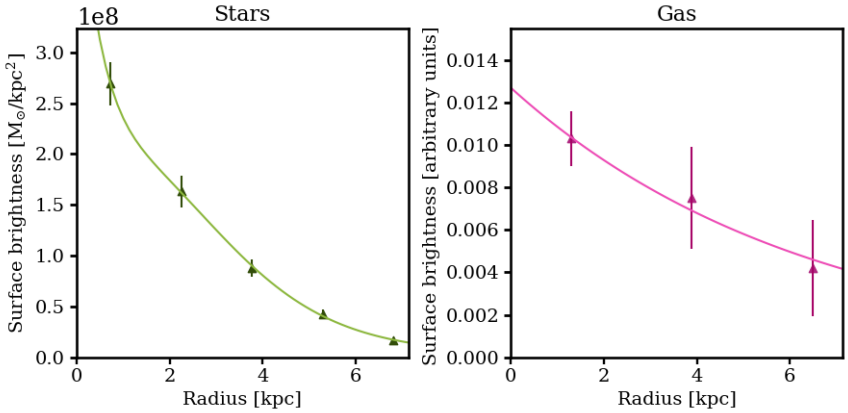

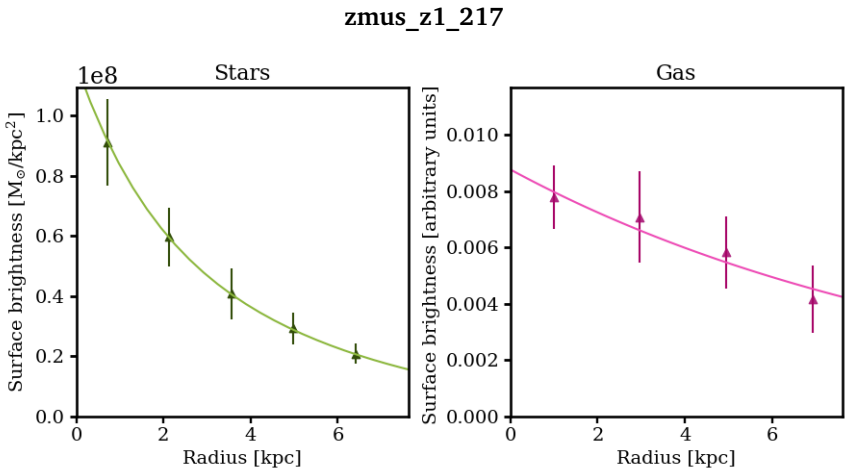

Figure A.2: Left panels: stellar surface brightness profiles from Marasco et al. 2019, fitted with poly-exponential functions. Right panels: Hα surface brightness profiles, obtained in this work and fitted with exponential functions.